

---

# Learning Graph Embeddings on Constant-Curvature Manifolds for Change Detection in Graph Streams

---

**Daniele Grattarola**

Faculty of Informatics  
Università della Svizzera italiana  
6900 Lugano, Switzerland  
daniele.grattarola@usi.ch

**Daniele Zambon**

Faculty of Informatics  
Università della Svizzera italiana  
6900 Lugano, Switzerland  
daniele.zambon@usi.ch

**Cesare Alippi**

Università della Svizzera italiana  
6900 Lugano, Switzerland  
Politecnico di Milano  
20133 Milano, Italy  
cesare.alippi@usi.ch

**Lorenzo Livi**

Department of Computer Science  
University of Exeter  
Exeter EX4 4QF, United Kingdom  
l.livi@exeter.ac.uk

## Abstract

The space of graphs is characterized by a non-trivial geometry, which often complicates performing inference in practical applications. A common approach is to use embedding techniques to represent graphs as points in a conventional Euclidean space, but non-Euclidean spaces are often better suited for embedding graphs. Among these, constant curvature manifolds (CCMs), like hyperspheres and hyperboloids, offer a computationally tractable way to compute metric, yet non-Euclidean, geodesic distances. In this paper, we introduce a novel adversarial graph embedding technique to represent graphs on CCMs, and exploit such a mapping for detecting changes in stationarity in a graph-generating process. To this end, we introduce a novel family of change detection tests operating by means of distances on CCMs. We perform experiments on synthetic graph streams, and on sequences of functional networks extracted from iEEG data with the aim of detecting the onset of epileptic seizures. We show that our methods are able to detect extremely small changes in the graph-generating process, consistently outperforming solutions based on Euclidean embeddings. The general nature of our framework highlights its potential to be extended to other applications characterized by graph data or non-Euclidean geometries.

## 1 Introduction

Many relevant machine learning applications require to go beyond conventional Euclidean geometry, as in the case of data described by attributed graphs [31, 6]. When studying problems on graphs, one of the key issues is to find representations that allow dealing with their underlying geometry, which is usually defined by application-specific distances that often do not satisfy the triangular inequality [22, 37]. The use of metric distances, like graph alignment distances [14], only mitigates the problem, as they are computationally intractable. Therefore, a common approach is to embed graphs on a more conventional geometric space, such as the Euclidean one. However, Euclidean geometry is not always the optimal choice, even when using metric distances, as graphs may find a natural representation on non-Euclidean domains [40]. To this end, constant-curvature manifolds (CCMs), like hyperspherical and hyperbolic spaces, offer a first approximation of non-Euclidean

geometry that preserves a metric structure (i.e., geodesics are metric and can be easily computed in closed-form), and therefore are suitable to be used in inference procedures. Moreover, CCMs have the advantage of being parametrized by a scalar, the curvature, which completely determines their geometry [37].

Representing graphs as points in metric spaces yields significant benefits when dealing with problems that require studying their statistical properties. For instance, in many application scenarios (as those dealing with analysis of complex networks [26]), graphs are assumed to be generated by a stationary process, implying that neither the edges nor the graph attributes are drawn from a time-variant distribution. However, the stationarity assumption does not always hold true, with relevant examples including cyber-physical systems [1], functional networks associated with brain imaging (where neural activity changes over time autonomously, or by reaction to stimuli) [13], and many others, e.g., see [10, 25, 19, 21].

In this paper, we focus on the rather unexplored problem of detecting changes in stationarity of a process generating attributed graphs (see [39] for a literature review). We show that, by representing graphs on CCMs, we obtain a significant performance improvement w.r.t. to Euclidean representations. The contributions of this work are twofold. First, we propose to use a graph autoencoder (GAE) [35, 16] to embed graphs on a CCM. We introduce a novel approach based on the adversarial autoencoder framework [23] to impose a geometric constraint on a GAE’s latent space, by matching the aggregated posterior of the GAE with a prior defined on a CCM. By enforcing a prior with support on the CCM, we are able to progressively impose the geometric constraint (i.e., bounding embeddings to lie on the manifold), as the GAE will learn to embed on the CCM in order to fool the discriminator network. We also propose a variation of this algorithm that operates without a prior distribution, enforcing the geometric constraint through adversarial learning with a simple, parameter-free discriminator, hence significantly reducing the overall model complexity. We consider hyperspherical and hyperbolic CCMs, as well as an ensemble of different geometries (Euclidean, spherical, and hyperbolic), learned by jointly optimizing the embedded representation on CCMs characterized by different curvatures. The second contribution of this paper consists in a novel family of change detection tests (CDTs) operating on CCMs. The first proposed CDT considers the geodesic distances of each embedded graph w.r.t. the sample Fréchet mean observed in the nominal regime of the process. The resulting stream of distances is processed by a CDT based on the Central Limit Theorem (CLT). The second method considers embeddings directly on the CCMs, and builds on a novel CDT based on the CLT for Riemannian manifolds [4].

We report an extensive comparative analysis of the developed embedding and change detection mechanisms, by testing our architecture on both synthetic data and a real-world seizure detection/prediction problem. We show that our methodology is able to effectively exploit the non-Euclidean geometry of CCMs to detect changes in graph streams, even in the case of extremely small changes, consistently outperforming baseline algorithms. The ensemble of CCMs and the parameter-free discriminator are shown to almost always perform better than the other configurations, on all problems.

## 2 Background

### 2.1 Constant-curvature manifolds

A constant-curvature manifold  $\mathcal{M}_\kappa$  is a Riemannian manifold characterized by a sectional curvature  $\kappa \in \mathbb{R}$ , constant over the entire manifold. We have three different geometries: Euclidean ( $\kappa = 0$ ), spherical ( $\kappa > 0$ ), and hyperbolic ( $\kappa < 0$ ). The Euclidean manifold  $\mathcal{M}_0$  is equipped with distance  $\rho_0(\mathbf{x}_1, \mathbf{x}_2) = \|\mathbf{x}_1 - \mathbf{x}_2\|_2$ . For  $\kappa > 0$ ,  $\mathcal{M}_\kappa$  is a sphere of radius  $r = \kappa^{-1/2}$ . Here, by defining the Euclidean inner product as  $\langle \mathbf{x}_1, \mathbf{x}_2 \rangle_\kappa = \mathbf{x}_1^\top \mathbf{x}_2 = \sum \mathbf{x}_{1j} \mathbf{x}_{2j}$ , the geodesic distance becomes  $\rho_\kappa(\mathbf{x}_1, \mathbf{x}_2) = \kappa^{-1/2} \arccos(\kappa \langle \mathbf{x}_1, \mathbf{x}_2 \rangle_\kappa)$ . We comment that points on a  $d$ -dimensional sphere are represented as  $d + 1$ -dimensional real vectors satisfying  $\langle \mathbf{x}, \mathbf{x} \rangle_\kappa = \kappa^{-1}$ . Accordingly, we say that the manifold is *embedded* in  $\mathbb{R}^{d+1}$ , also called the *host space*. A hyperbolic manifold has a less intuitive description, as its geometrical properties derive from a pseudo-Euclidean space, i.e., a non metric vector space equipped with scalar product  $\langle \mathbf{x}_1, \mathbf{x}_2 \rangle_\kappa = \sum_{j=1}^d \mathbf{x}_{1,j} \mathbf{x}_{2,j} - \mathbf{x}_{1,d+1} \mathbf{x}_{2,d+1}$  [30]. Again, a point on a hyperbolic manifold is represented by  $d + 1$  real coordinates constrained by  $\langle \mathbf{x}, \mathbf{x} \rangle_\kappa = \kappa^{-1}$ ; the associated geodesic metric is  $\rho_\kappa(\mathbf{x}_1, \mathbf{x}_2) = (-\kappa)^{-1/2} \operatorname{arccosh}(\kappa \langle \mathbf{x}_1, \mathbf{x}_2 \rangle_\kappa)$ .

## 2.2 Probability distributions on CCMs

Given a Riemannian manifold  $\mathcal{M}$ , and a tangent space  $T_x\mathcal{M}$ , we denote with  $\text{Exp}_x(\cdot)$  the *Riemannian exponential map* (exp-map) [36]; the point of tangency  $x$  is called the *origin* of the map.  $\text{Exp}_x(\cdot)$  maps points from  $T_x\mathcal{M}$  to  $\mathcal{M}$ . The exp-map inverse  $\text{Log}_x(\cdot)$ , or *log-map*, maps points from the manifold to the tangent space.  $\text{Exp}_x(\cdot)$  and  $\text{Log}_x(\cdot)$  have the property of preserving the distances from the origin. That is, given a point  $P$  on the manifold and  $Q = \text{Log}_x(P)$ , we have  $\rho_{\mathcal{M}}(P, x) = d_e(Q, x)$ , where  $\rho_{\mathcal{M}}(\cdot, \cdot)$  is the geodesic distance on the manifold, and  $d_e(\cdot, \cdot)$  is the Euclidean distance operating on the tangent space.

Following [36], we use the exp-map and log-map operators to define a probability distribution on a manifold. In particular, given a probability distribution  $P(\theta)$  on the tangent space  $T_x\mathcal{M}$ , parametrized in vector  $\theta$ , we define the distribution  $\text{Exp}_x(P(\theta))$ , obtained by first sampling a point in  $T_x\mathcal{M}$  from  $P(\theta)$ , and then mapping it to  $\mathcal{M}$  using  $\text{Exp}_x(\cdot)$ ; distribution  $\text{Exp}_x(P(\theta))$  is called the *push-forward* distribution of  $P(\theta)$  through  $\text{Exp}_x(\cdot)$ . In the case of CCMs with  $\kappa \neq 0$ , we always choose as origin the point  $x \in \mathbb{R}^{d+1}$  with  $x_i = 0, i = 1, \dots, d$ , and  $x_{d+1} = |\kappa|^{-1/2}$ , and refer to the push-forward distribution as  $P_{\mathcal{M},\kappa}(\theta)$ .

## 2.3 Adversarial autoencoders

Adversarial autoencoders (AAEs) [23] are probabilistic models trained using the generative adversarial networks framework proposed by [12]. AAEs perform variational inference by matching the aggregated posterior of an autoencoder’s (AE) latent space with a prior distribution  $p(\mathbf{z})$ . In AAEs, the encoder network of the AE acts as the generator, and is trained to fool the discriminator network  $D(\mathbf{z})$  to think that samples from the encoder come from the prior distribution.

The training procedure for AAEs consists in a *reconstruction* phase and a *regularization* phase. In the reconstruction phase, the AE is trained to reconstruct input samples from the data distribution. In the regularization phase,  $D(\mathbf{z})$  is initially trained to distinguish between samples coming from the prior  $p(\mathbf{z})$  and those produced by the encoder. The encoder is then updated to maximize the classification error of the discriminator. At the end of the training procedure, the decoder can be used as generative model to map the latent space to the data distribution, whereas the encoder will have an aggregated posterior ideally indistinguishable from the true prior.

## 3 Change detection with graph embeddings on CCMs

We consider the task of determining whether the probability distribution underlying a graph-generating process has changed, from a *nominal* stationary distribution  $Q_0$  to a *non-nominal* distribution  $Q_1$ . Our methodology consists in using an adversarially regularized graph autoencoder to compute graph embeddings on a CCM, and then exploiting the simplified geometry of the embedding space to run a change detection test. The algorithm is split between a *training* and an *operational* phase. In the training phase, we observe a finite stream of graphs  $G_{train}$  coming from the nominal regime, which we use to train the GAE. The stream is then mapped to the CCM  $\mathcal{M}_\kappa$  using the encoder network of the GAE, and a statistical analysis of  $Q_0$  is performed there, in order to configure a threshold for the CDT (details in Sec. 3.2). In the operational phase, we monitor the graph-generating process, again mapped to the CCM using the encoder, with the aim of raising an *alarm* when a change in stationarity is detected. In the following sections, we describe in detail both the embedding procedure on CCMs and the proposed CDT techniques.

### 3.1 Adversarial graph embeddings on CCMs

A graphical illustration of the proposed architecture is provided in Fig. 1. We consider graphs with a fixed number  $N$  of identified nodes,  $F$ -dimensional node attributes, and  $S$ -dimensional edge attributes.<sup>1</sup> Graphs are represented as tuples  $g = (A, X, E)$ , where  $A \in \{0, 1\}^{N \times N}$  is the adjacency matrix,  $X \in \mathbb{R}^{N \times F}$  represents node attributes, and  $E \in \mathbb{R}^{N \times N \times S}$  represents edge attributes. The encoder network of the GAE is obtained by stacking graph convolutions [17, 9], which learn a representation of input graphs by exploiting  $A$  and  $E$  to transform  $X$  (see Eq. (2)). The decoder network, then, is trained to reconstruct all three input matrices from the latent representation only.

<sup>1</sup>Graphs with less than  $N$  nodes can be considered by adding dummy nodes.

In order to learn a representation on a CCM  $\mathcal{M}_\kappa$ , we set the latent space of the GAE to be the host space of  $\mathcal{M}_\kappa$ , and constrain the embeddings to lie exactly on the CCM. We achieve this *manifold regularization* by training our GAE adversarially on the sequence of nominal graphs  $G_{train}$ , conditioning its aggregated posterior to match a prior distribution  $P_{\mathcal{M}_\kappa}$  with support on  $\mathcal{M}_\kappa$ . Such a prior allows us to implicitly define the geometric constraints that we wish to impose on the latent space, so that the representation on the CCM can be autonomously learned by the adversarially regularized GAE. In order to constrain the embeddings without conditioning the aggregated posterior, we also propose an alternative AAE setting, in which a parameter-free discriminator is used to compute the membership of an embedding to the CCM (details in Sec. 3.1.2).

Training the GAE adversarially yields a good performance in constraining the latent space to  $\mathcal{M}_\kappa$ , but does not guarantee that all embeddings lie *exactly* on the CCM (hence making it impossible to compute geodesics). To compensate for the GAE’s error, we introduce a clipping function that projects embeddings  $\mathbf{z}$  onto  $\mathcal{M}_\kappa$ .<sup>2</sup>

$$\text{clip}_{\mathcal{M}_\kappa}(\mathbf{z}) = \begin{cases} \frac{\mathbf{z}}{\sqrt{\kappa \|\mathbf{z}\|}} & \text{if } \kappa > 0, \\ \mathbf{z} & \text{if } \kappa = 0, \\ \left[ z_1, \dots, z_d, \sqrt{\sum_{j=1}^d z_j^2 - \frac{1}{\kappa}} \right] & \text{if } \kappa < 0. \end{cases} \quad (1)$$

In the following sections, we provide details on the implementation of the adversarial GAE.

### 3.1.1 Graph autoencoder: model and loss

For the encoder network  $\text{ENC} : \mathcal{G} \rightarrow \mathbb{R}^{c(d+1)}$ , we stack edge-conditioned convolution (ECC) layers [34], each of which computes a transformed signal  $X^{(l)} \in \mathbb{R}^{N \times F_l}$  from an input signal  $X^{(l-1)} \in \mathbb{R}^{N \times F_{l-1}}$ . Given a graph  $g = (A, X, E)$ , an ECC layer computes for each node  $i$  of  $g$ :

$$X_{i,\cdot}^{(l)} = \frac{A_{i,\cdot}}{\sum_j A_{ij}} f(E_{i,\cdot,\cdot}; \theta^{(l)}) X_{i,\cdot}^{(l-1)} + b^{(l)}, \quad (2)$$

where  $f : \mathbb{R}^S \rightarrow \mathbb{R}^{F_l \times F_{l-1}}$  is a *filter generating network*, parametrized by  $\theta^{(l)}$ , that outputs convolution filters as a function of edge attributes, and  $b^{(l)}$  is a bias vector. ECCs allow us to exploit information associated with both nodes and edges, although any choice of encoder would be equally suitable here. We include a global attention pooling layer [20, 35] after the last convolutional one,

<sup>2</sup>Note that (1) only projects the embeddings when  $\kappa_i \neq 0$ . Since the distance on the Euclidean space is well defined on  $\mathbb{R}^{d+1}$ , we prefer to introduce an additional degree of freedom to the Euclidean representation rather than constraining the embeddings to have a constant coordinate.

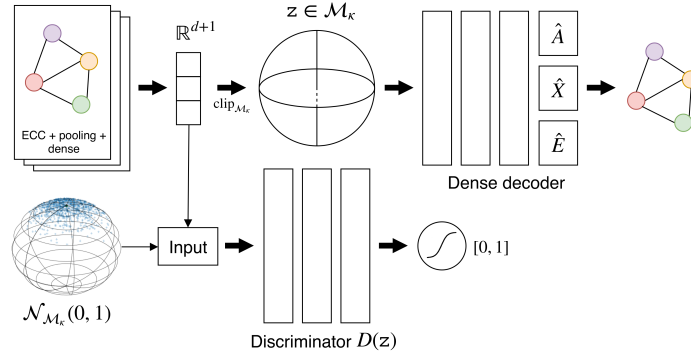


Figure 1: Schematic view of the adversarial GAE with a spherical CCM. The GAE is composed of an ECC encoder producing embeddings on  $\mathbb{R}^{d+1}$ , which are then exactly projected on  $\mathcal{M}_\kappa$  via  $\text{clip}_{\mathcal{M}_\kappa}(\cdot)$ , and a dense decoder producing the adjacency and attribute matrices. The discriminator is trained to distinguish between the prior  $\mathcal{N}_{\mathcal{M}_\kappa}(0, 1)$  and the encoder’s posterior.

followed by a fully connected layer to produce the latent representation on the CCM. Embeddings are projected onto  $\mathcal{M}_\kappa$  using (1) before being fed to the decoder, and we explicitly distinguish between the embeddings before and after the projection step by defining the *clipped* encoder  $\text{ENC}_{\text{clip}} : \mathcal{G} \rightarrow \mathcal{M}_\kappa$ , where  $\text{ENC}_{\text{clip}}(\cdot) = \text{clip}_{\mathcal{M}_\kappa}(\text{ENC}(\cdot))$ . The decoder,  $\text{DEC} : \mathcal{M}_\kappa \rightarrow \mathcal{G}$ , is a fully connected neural network with three parallel output layers producing the reconstructed adjacency matrix  $\hat{A}$ , node attributes  $\hat{X}$ , and edge features  $\hat{E}$ . In the reconstruction phase, we train the GAE to minimize the reconstruction loss:

$$L = -\frac{1}{N^2} \sum_{i,j} A_{ij} \log \hat{A}_{ij} + \|X - \hat{X}\|_{\text{F}}^2 + \|E - \hat{E}\|_{\text{F}}^2. \quad (3)$$

### 3.1.2 Discriminator and adversarial regularization

For the regularization phase, we consider a discriminator network  $D(\mathbf{z})$ , outputting the probability that a point  $\mathbf{z} \in \mathbb{R}^{d+1}$  is a sample from the prior  $P_{\mathcal{M}_\kappa}$ , rather than an embedding produced by the encoder. We train the discriminator using samples from  $P_{\mathcal{M}_\kappa}$  as positive examples, and embeddings from  $\text{ENC}(\cdot)$  as negative examples. We then freeze the weights of the discriminator and train the composition  $D(\text{ENC}(\cdot))$  using only graphs from the data distribution as positive examples. We comment that enforcing a user-defined distribution on the encoder’s representation is not our primary goal. Moreover, the model complexity of the adversarial architecture is a disadvantage on problems characterized by a scarcity of data (like the seizure detection task detailed in Sec. 5). Therefore, we propose a variation of the adversarial GAE that, while significantly reducing the number of parameters in the model, still achieves the desired manifold regularization. We introduce a parameter-free *geometric* discriminator for a CCM  $\mathcal{M}_\kappa$ , defined as:

$$D_{\mathcal{M}_\kappa}(\mathbf{z}) = \begin{cases} \exp\left(\frac{-\left(\langle \mathbf{z}, \mathbf{z} \rangle - \frac{1}{\kappa}\right)^2}{2\varsigma^2}\right) & \text{if } \kappa_i \neq 0 \\ 1 & \text{if } \kappa_i = 0, \end{cases} \quad (4)$$

where  $\varsigma$  is a hyperparameter that controls the softness of the classifier. Intuitively, this model defines a surface where  $D_{\mathcal{M}_\kappa}(\mathbf{z}) = 1$  when the embeddings lie exactly on  $\mathcal{M}_\kappa$ , and  $D(\mathbf{z}) \rightarrow 0$  when they are distant from it. This achieves the desired manifold regularization without imposing an explicit distribution on the embeddings. In this case, we skip the first step of the AAE regularization phase (since we do not need to match the prior anymore) and only train  $D_{\mathcal{M}_\kappa}(\text{ENC}(\cdot))$ , updating the encoder to confuse the geometric discriminator.

## 3.2 Change detection on CCMs

The test hypotheses for detecting a change in stationarity in the distribution of a graph stream  $\{g_1, g_2, \dots, g_i, \dots\}$  are

$$H_0 : g_i \sim Q_0, \quad i = 1, 2, \dots, \quad H_1 : g_i \sim \begin{cases} Q_0 & i < \tau \\ Q_1 & i \geq \tau, \end{cases}$$

with  $\{g_i\}$  statistically independent, and where  $\tau$  is the *change point* of the stream. Note that both  $Q_0$  and  $Q_1$  are unknown. During the operational phase, we use the clipped encoder network to convert the incoming graph stream into the multivariate stream  $\{\mathbf{z}_1, \mathbf{z}_2, \dots, \mathbf{z}_i, \dots \mid \mathbf{z}_i \in \mathcal{M}_\kappa\}$ , which is monitored by a sequential statistical test to detect a possible change in the driving distribution. Accordingly, the graph stream  $G_{\text{train}}$ , with which we trained the GAE, is converted to a stream of embeddings  $Z_{\text{train}}$ .

Our change detection methodology builds on the CDT proposed by Zambon et al. [39], by extending it to the case of CCMs. The approach of [39] considers a generic stream of points  $\{u_1, u_2, \dots, u_i, \dots\}$ , which is processed in windows of  $n$  points at a time, so that for each  $w = 1, 2, 3, \dots$  a window  $[u]_w = \{u_{(w-1)n+1}, \dots, u_{wn}\}$  is generated, and a statistic  $S_w$  is computed by the accumulation process typical of the cumulative sums (CUSUM) chart [28]. Statistic  $S_w$  has a global role, as it accumulates information from *local* statistics  $s_i = s([u]_i)$ , for  $i = 1, \dots, w$ , recurrently as  $S_w = \max\{0, S_{w-1} + s_w - q\}$ , with  $S_0 = 0$  and  $q$  a parameter tuning the sensitivity of the test. The null hypothesis  $H_0$  is rejected the first time  $S_w$  exceeds a threshold  $h_w$ , and the change point is estimated as  $\hat{\tau} = n \cdot \min\{w \mid S_w > h_w\}$ . Threshold  $h_w$  is set according to a user-defined significance

level  $\alpha$ , by requiring, under the null hypothesis  $H_0$ , that  $\mathbb{P}(S_w > h_w | H_0, S_i \leq h_i, i < w) = \alpha$ . The threshold is set so that the probability of having a false alarm at generic step  $w$  is  $\alpha$ , hence allowing us to control the false positive detection rate. Note that the scoring function  $s_w = s([u]_w)$  entirely defines the behavior of the CDT, and that by knowing the distribution of  $s_w$  we can compute the threshold  $h_w$  given  $\alpha$ . Here, we consider  $s_w$  to be the Mahalanobis distance

$$s_w = (\mathbb{E}[u] - \overline{[u]_w})^\top \text{Cov}[u]^{-1} (\mathbb{E}[u] - \overline{[u]_w}), \quad (5)$$

between the sample mean  $\overline{[u]_w}$  of  $[u]_w$  and the expected value of  $u$ . In the stationary case, thanks to the central limit theorem (CLT), it can be shown that  $n \cdot s_w \sim \chi^2$ . We propose two different choices of  $u$  that exploit the geometry of the CCMs.

**Distance-based CDT (D-CDT)** The first proposed CDT considers the nominal distribution  $F_0$  of  $\mathbf{z}_i$ , derived as the push-forward distribution of  $Q_0$  through  $\text{ENC}_{\text{clip}}$  (c.f. Section 2.2). The Fréchet mean of  $F_0$ , denoted  $\mu_0$ , is estimated over the training sequence  $Z_{\text{train}}$  as

$$\mu_0 = \arg \min_{\mathbf{z}} \sum_{\mathbf{z}' \in Z_{\text{train}}} \rho(\mathbf{z}', \mathbf{z})^2. \quad (6)$$

For each embedding  $\mathbf{z}_i \in \mathcal{M}_\kappa$ , then, we consider  $u_i = \rho_\kappa(\mu_0, \mathbf{z}_i)$ , and the resulting sequence  $\{u_1, u_2, \dots, u_i, \dots\}$  is finally monitored with the basic CDT presented above.

**Riemannian CLT-based CDT (R-CDT)** Our second implementation of the CDT builds on a Riemannian version of the CLT proposed in [4], which adapts the Mahalanobis distance (5) to deal with non-Euclidean manifolds. In this case, the stream of embedded graphs on  $\mathcal{M}_\kappa$  is mapped to the tangent space  $T_{\mu_0} \mathcal{M}_\kappa$  s.t.  $u_i = \text{Log}_{\mu_0}(\mathbf{z}_i)$ , and the base CDT is applied by using the modified local statistic  $s_w$ . In the case of  $\kappa = 0$ , the usual CLT applies directly to the embeddings without modifications of  $s_w$ .

### 3.3 Ensemble of CCMs

In most applications we do not have priors about the optimal CCM. To this end, we propose an ensemble of CCMs, each characterized by a different geometry, or by the same geometry but different curvatures. The ensemble of CCMs is in the form  $\mathcal{M}_* = \mathcal{M}_{\kappa_1} \times \dots \times \mathcal{M}_{\kappa_i} \times \dots \times \mathcal{M}_{\kappa_c}$ , and the GAE is trained to jointly optimize the representation directly on  $\mathcal{M}_*$ . Adapting the GAE to the ensemble of CCMs is as simple as considering  $c$  parallel fully connected layers after pooling, each producing a representation in a  $d + 1$ -dimensional host space. The produced embeddings are then concatenated in a single  $c(d + 1)$ -dimensional vector before being fed to the decoder and the discriminator. In order to constrain the combined latent space to  $\mathcal{M}_*$ , we define a prior  $P_{\mathcal{M}_*}$ , where a sample  $\mathbf{z} \sim P_{\mathcal{M}_*}$  is the concatenation of  $c$  samples  $\mathbf{z}_i \in \mathbb{R}^{d+1}$ , drawn from distributions  $P_{\mathcal{M}_{\kappa_i}}$  with support on each CCM. In the case of the geometric discriminator, given an embedding  $\mathbf{z}$ , we apply a geometric classifier  $D_{\mathcal{M}_{\kappa_i}}$  to its  $c$  consecutive slices  $\mathbf{z}_i \in \mathbb{R}^{d+1}$ , and compute the average as  $D_{\mathcal{M}_*}(\mathbf{z}) = c^{-1} \sum_{i=1}^c D_{\mathcal{M}_{\kappa_i}}(\mathbf{z}_i)$ . Similarly, the projection of  $\mathbf{z}$  onto  $\mathcal{M}_*$  reads  $\text{clip}_{\mathcal{M}_*}(\mathbf{z}) = \left\|_{i=1}^c \text{clip}_{\mathcal{M}_{\kappa_i}}(\mathbf{z}_i)\right\|$ , where  $\left\|$  represents the concatenation of vector slices.

Accordingly, we also adapt the CDTs described in Sec. 3.2 to consider the different CCMs. For D-CDT, we consider each CCM separately, and for each compute the same distance-based representation as the single CCM case. This results in a multivariate stream of  $c$ -dimensional distance vectors, which can be monitored by the base CDT. Similarly, R-CDT is adapted by considering a R-CDT for each CCM  $\mathcal{M}_{\kappa_i}$ . The ensemble of statistical tests raises an alarm any time at least one of the individual tests detects a change. Since the tests are in general not independent, we apply a Bonferroni correction [5] to each R-CDT, so that the overall significance level is at least the user-defined level  $\alpha$ .

## 4 Related work

In this section, we focus on recent literature regarding unsupervised *geometric deep learning* [6] and related embeddings on Riemannian manifolds. GAEs are typically used to encode the topological structure and node content of a single graph [16, 3, 32]; in this framework, an adversarially regularized GAE is proposed by Pan et al. [29]. Closer to our approach, Simonovsky and Komodakis [35]

propose a graph variational autoencoder (GVAE) operating on batches of graphs rather than on a single network. Their architecture focuses on variational inference for generating molecules, and adds a graph matching step between the input and reconstructed samples in order to support unidentified nodes. Davidson et al. [8] introduces a GVAE based on the von Mises - Fisher distribution, aimed at modeling the spherical geometry underlying directional data (e.g., data with natural support of a hypersphere). Korman [18] proposes to use the AAE framework to recover the manifold underlying a data distribution, without making assumptions on the geometry of the manifold. This is achieved by approximating the manifold as a set of *charts*, each represented by the latent space of a linear AAE trained to match a uniform prior. The Riemannian geometry of deep generative models is also studied in [33] and [7], whereas [11] studies the metric-preserving properties of neural networks with random Gaussian weights. In order to capture the hierarchical structure of domains like natural language, Nickel and Kiela [27] develop a technique based on stochastic gradient descent on manifolds for embedding graph data on a *Poincaré ball*.

## 5 Experiments

### 5.1 Data and application scenarios

**Delaunay triangulations** We follow the approach in [38] to test our architecture on a synthetic problem. In this setting, a graph is generated by computing the Delaunay triangulation of a set of points in  $\mathbb{R}^2$ , and the coordinates of the points are used as node attributes. A class of graphs is defined by a fixed set of  $N = 7$  support points, and graph instances are generated by adding Gaussian noise. By changing the support points, we are able to generate different classes of graphs. We distinguish between the nominal class 0, and the non-nominal classes  $i = 1, \dots, 20$ , generated by perturbing the support of class 0. To generate a stream, we sample graphs of class 0 in the nominal regime, and simulate a change by transitioning to a different class  $i$  for the non-nominal regime. This allows us to have a ground truth with a known change point.

**iEEG data** We also test our methodology on a real-world scenario, using intracranial EEG (iEEG) data from Kaggle’s *UPenn and Mayo Clinic’s Seizure Detection Challenge* (SDC) and the *American Epilepsy Society Seizure Prediction Challenge* (SPC). In these datasets, iEEG signals are provided in one-second clips belonging to two different classes, namely the nominal *interictal* samples and the non-nominal *ictal* (or *pre-ictal*, in the SPC case) samples. The datasets are collected from dogs and human patients, with a variable number of sensors applied to each patient, resulting in multivariate streams of different dimensions. Functional connectivity networks are widely used in neuroscience [2] to represent the coupling between activity of (macro-)units. Functional networks find a natural representation as weighted graphs, giving rise to a stream of attributed graphs, hence making the problem a suitable case study to test the proposed CDT methodology. Details of the Delaunay and iEEG datasets are provided in Appendix A.

### 5.2 Experimental setting

We consider three different CCMs, namely the Euclidean  $\mathcal{M}_0$ , hyper-spherical  $\mathcal{M}_1$ , and hyperbolic  $\mathcal{M}_{-1}$  manifolds, and for all CCMs we take  $d = 2$ . Since we are unable to identify a priori the best curvature, we also consider an ensemble of all three geometries,  $\mathcal{M}_* = \mathcal{M}_{-1} \times \mathcal{M}_0 \times \mathcal{M}_1$ . We test each manifold with both the standard AAE formulation (i.e., with a Gaussian prior  $\mathcal{N}_{\mathcal{M}_{\kappa_i}}(0, 1)$ ) and the one using the geometric discriminator (4), as well as apply both D-CDT and R-CDT. Configuration details for the GAE, the discriminators, and the training procedure are reported in Appendix B, whereas for the CDTs we set  $\alpha = 0.01$  and  $q = 0.75$ . The reference baseline is that of Zambon et al. [39], for which we use the open-source implementation published by the authors, with a  $d + 1$ -dimensional dissimilarity representation. As performance metric, we adapt AUC to the change detection problem, as discussed in Appendix C.

### 5.3 Results

**Delaunay triangulations** We report in Table 1, for each CCM, the best result for the tested system configurations. Results show that the combination of geometric discriminator and R-CDT on  $\mathcal{M}_*$  consistently outperforms all other methods. This suggests that CCMs with different curvatures encode

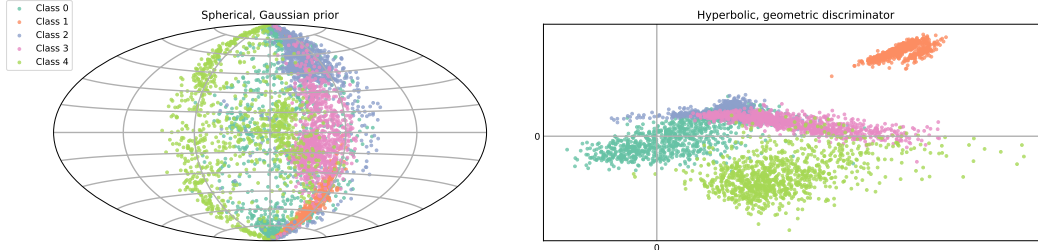


Figure 2: Hammer and planar projections of the first five Delaunay classes for CCMs  $\mathcal{M}_1$  and  $\mathcal{M}_{-1}$ , respectively, using the GAE configurations reported in Table 1 (best viewed in color).

Table 1: AUC score on Delaunay triangulations (best results are in bold). The *Emb.* column indicates whether the embeddings were computed using the standard AAE setting with a prior, or the geometric discriminator (4). Class indices are proportional to the difficulty in detecting the change (c.f. Appendix A). The baseline by [39] is indicated as using R-CDT because it is formally equivalent to a R-CDT on Euclidean manifolds.

		Class in non-nominal regime										
CCM	CDT	Emb.	20	18	16	14	12	10	8	6	4	2
$\mathcal{M}_*$	R-CDT	Geom	<b>0.70</b>	<b>0.71</b>	<b>0.74</b>	<b>0.76</b>	<b>0.78</b>	<b>0.73</b>	<b>0.98</b>	<b>0.96</b>	<b>1.00</b>	<b>1.00</b>
$\mathcal{M}_{-1}$	R-CDT	Geom	0.54	0.61	0.51	0.66	0.57	0.58	0.63	0.67	<b>1.00</b>	0.93
$\mathcal{M}_0$	D-CDT	Prior	0.47	0.52	0.55	0.64	0.59	0.60	0.91	0.95	0.99	<b>1.00</b>
$\mathcal{M}_1$	R-CDT	Prior	0.45	0.50	0.53	0.59	0.55	0.50	0.79	0.77	<b>1.00</b>	0.99
$\mathcal{M}_0$	R-CDT	[39]	0.49	0.50	0.50	0.50	0.50	0.52	0.56	0.88	0.93	0.93

different yet useful information, which the algorithm is able to exploit. A graphical illustration of the latent space learned by the GAE is shown in Fig. 2. Moreover, we note a considerably high performance in those problems characterized by a less evident change, where the algorithm is able to detect data perturbations in the order of  $10^{-3}$  (see Appendix A for details). We also note that, while performing comparably to the standard AAE formulation in different configurations, the geometric discriminator still provides noticeable benefits on model complexity, particularly for smaller  $N$  (as the complexity of the GAE is quadratic w.r.t.  $N$ ). Here, for instance, we notice a significant reduction of up to 13.35% in the total number of parameters (i.e., from  $\approx 252k$  to  $\approx 218k$ ) w.r.t. using the standard discriminator.

**iEEG data** The proposed method denotes a similarly good performance on iEEG data, where the CCM ensemble, with R-CDT and the geometric discriminator, outperforms single-curvature geometries and the baseline on most patients. Details of the results are reported in Table 2. We notice that the spherical CCM denotes a marginal advantage w.r.t. the other configurations on P1, indicating that single CCMs can be effective in some cases. We also notice the poor performance achieved by all configurations on subject P2. Here, when considering pre-ictal graphs, the representation learned by the encoder collapses around the mean value of nominal regime, resulting in a poor detection performance. The benefits of the geometric discriminator on SDC and SPC are less evident than what obtained on synthetic data (due to the graphs having more nodes), but still amount to a significant reduction in the number of parameters of 5% on average.

Experimental results for both application scenarios are reported in full detail in Appendix D.

## 6 Conclusion

In this paper, we introduced a novel technique for embedding graphs on constant curvature manifolds, and showed its effectiveness for detecting changes in streams of graph-structured data, on both synthetic and real-world applications. We showed that leveraging different geometries ( $\mathcal{M}_*$ ), using the geometric discriminator and R-CDT, consistently yields the best performance, making this configuration a safe choice where no prior information is given about the problem. We believe that the



Table 2: AUC score on iEEG data, where D and P indicate subjects from the SDC and SPC datasets, respectively (details in Appendix A). Best results are in bold.

CCM	CDT	Emb.	D1	D2	D3	D4	D5	D6	D7	P1	P2	P3
$\mathcal{M}_*$	R-CDT	Geom.	<b>1.00</b>	<b>1.00</b>	<b>1.00</b>	<b>0.94</b>	<b>1.00</b>	0.74	<b>1.00</b>	0.54	0.51	<b>0.97</b>
$\mathcal{M}_{-1}$	D-CDT	Geom.	<b>1.00</b>	0.99	0.99	<b>0.94</b>	0.99	0.62	<b>1.00</b>	0.64	0.25	0.85
$\mathcal{M}_0$	D-CDT	Prior	0.99	0.99	0.99	0.74	0.97	0.59	0.99	0.76	0.10	0.90
$\mathcal{M}_1$	D-CDT	Prior	0.99	0.99	0.99	0.90	0.99	0.33	0.98	<b>0.87</b>	0.48	0.82
$\mathcal{M}_0$	R-CDT	[39]	0.92	0.74	0.84	0.90	0.90	<b>0.88</b>	0.79	0.73	<b>0.84</b>	0.90

proposed techniques can be extended beyond the scope considered in this paper, as many application domains are characterized by graph-structured data, such as sensor and gene expression networks.

## Acknowledgments

This research is funded by the Swiss National Science Foundation project 200021\_172671: “ALPS-FORT: A Learning graph-baSed framework FOr cybER-physical sysTems”.

## References

- [1] C. Alippi and M. Roveri. The (not) far-away path to smart cyber-physical systems: An information-centric framework. *Computer*, 50(4):38–47, 2017.
- [2] A. M. Bastos and J.-M. Schoffelen. A tutorial review of functional connectivity analysis methods and their interpretational pitfalls. *Frontiers in Systems Neuroscience*, 9:175, 2016. doi: 10.3389/fnsys.2015.00175.
- [3] R. v. d. Berg, T. N. Kipf, and M. Welling. Graph convolutional matrix completion. *arXiv preprint arXiv:1706.02263*, 2017.
- [4] R. Bhattacharya and L. Lin. Differential geometry for model independent analysis of images and other non-euclidean data: Recent developments. *arXiv preprint arXiv:1801.00898*, 2018.
- [5] C. Bonferroni. Teoria statistica delle classi e calcolo delle probabilita. *Pubblicazioni del R. Istituto Superiore di Scienze Economiche e Commerciali di Firenze*, 8:3–62, 1936.
- [6] M. M. Bronstein, J. Bruna, Y. LeCun, A. Szlam, and P. Vandergheynst. Geometric deep learning: Going beyond Euclidean data. *IEEE Signal Processing Magazine*, 34(4):18–42, 2017. doi: 10.1109/MSP.2017.2693418.
- [7] N. Chen, A. Klushyn, R. Kurle, X. Jiang, J. Bayer, and P. van der Smagt. Metrics for deep generative models. *arXiv preprint arXiv:1711.01204*, 2017.
- [8] T. R. Davidson, L. Falorsi, N. De Cao, T. Kipf, and J. M. Tomczak. Hyperspherical variational auto-encoders. *arXiv preprint arXiv:1804.00891*, 2018.
- [9] M. Defferrard, X. Bresson, and P. Vandergheynst. Convolutional neural networks on graphs with fast localized spectral filtering. In *Advances in Neural Information Processing Systems*, pages 3844–3852, 2016.
- [10] G. Ditzler, M. Roveri, C. Alippi, and R. Polikar. Learning in nonstationary environments: A survey. *IEEE Computational Intelligence Magazine*, 10(4):12–25, Nov. 2015. ISSN 1556-603X. doi: 10.1109/MCI.2015.2471196.
- [11] R. Giryes, G. Sapiro, and A. M. Bronstein. Deep neural networks with random Gaussian weights: A universal classification strategy? *IEEE Transactions on Signal Processing*, 64(13): 3444–3457, Jul. 2016. ISSN 1053-587X. doi: 10.1109/TSP.2016.2546221.
- [12] I. Goodfellow, J. Pouget-Abadie, M. Mirza, B. Xu, D. Warde-Farley, S. Ozair, A. Courville, and Y. Bengio. Generative adversarial nets. In *Advances in Neural Information Processing Systems*, pages 2672–2680, 2014.
- [13] S. Heitmann and M. Breakspear. Putting the “dynamic” back into dynamic functional connectivity. *Network Neuroscience*, pages 1–61, 2017. doi: 10.1162/NETN\_a\_00041.
- [14] B. J. Jain. On the geometry of graph spaces. *Discrete Applied Mathematics*, 214:126–144, 2016. doi: 10.1016/j.dam.2016.06.027.
- [15] D. P. Kingma and J. Ba. Adam: A method for stochastic optimization. *arXiv preprint arXiv:1412.6980*, 2014.
- [16] T. N. Kipf and M. Welling. Variational graph auto-encoders. *NIPS Workshop on Bayesian Deep Learning*, 2016.
- [17] T. N. Kipf and M. Welling. Semi-supervised classification with graph convolutional networks. In *International Conference on Learning Representations*, 2017.

- [18] E. O. Korman. Autoencoding topology. *arXiv preprint arXiv:1803.00156*, 2018.
- [19] A. Li, S. P. Cornelius, Y.-Y. Liu, L. Wang, and A.-L. Barabási. The fundamental advantages of temporal networks. *Science*, 358(6366):1042–1046, 2017. doi: 10.1126/science.aai7488.
- [20] Y. Li, D. Tarlow, M. Brockschmidt, and R. Zemel. Gated graph sequence neural networks. *arXiv preprint arXiv:1511.05493*, 2015.
- [21] Y. Li, R. Yu, C. Shahabi, and Y. Liu. Diffusion convolutional recurrent neural network: Data-driven traffic forecasting. In *International Conference on Learning Representations*, 2018.
- [22] L. Livi and A. Rizzi. The graph matching problem. *Pattern Analysis and Applications*, 16(3): 253–283, 2013. ISSN 1433-7541. doi: 10.1007/s10044-012-0284-8.
- [23] A. Makhzani, J. Shlens, N. Jaitly, and I. Goodfellow. Adversarial autoencoders. In *International Conference on Learning Representations*, 2016.
- [24] H. B. Mann and D. R. Whitney. On a test of whether one of two random variables is stochastically larger than the other. *The Annals of Mathematical Statistics*, pages 50–60, 1947.
- [25] N. Masuda and R. Lambiotte. *A Guide to Temporal Networks*. Series on Complexity Science. World Scientific Publishing Company, Singapore, 2016.
- [26] M. E. J. Newman. *Networks: An Introduction*. Oxford University Press, Oxford, UK, 2010.
- [27] M. Nickel and D. Kiela. Poincaré embeddings for learning hierarchical representations. In *Advances in Neural Information Processing Systems*, pages 6341–6350, 2017.
- [28] E. S. Page. Continuous inspection schemes. *Biometrika*, 41(1/2):100–115, 1954.
- [29] S. Pan, R. Hu, G. Long, J. Jiang, L. Yao, and C. Zhang. Adversarially regularized graph autoencoder. *arXiv preprint arXiv:1802.04407*, 2018.
- [30] E. Pełkalska and R. P. W. Duin. *The Dissimilarity Representation for Pattern Recognition: Foundations and Applications*. World Scientific, 2005.
- [31] J. Richiardi, S. Achard, H. Bunke, and D. Van De Ville. Machine learning with brain graphs: Predictive modeling approaches for functional imaging in systems neuroscience. *IEEE Signal Processing Magazine*, 30(3):58–70, 2013. doi: 10.1109/MSP.2012.2233865.
- [32] R. Selvan, T. Kipf, M. Welling, J. H. Pedersen, J. Petersen, and M. de Bruijne. Extraction of airways using graph neural networks. *arXiv preprint arXiv:1804.04436*, 2018.
- [33] H. Shao, A. Kumar, and P. T. Fletcher. The Riemannian geometry of deep generative models. *arXiv preprint arXiv:1711.08014*, 2017.
- [34] M. Simonovsky and N. Komodakis. Dynamic edge-conditioned filters in convolutional neural networks on graphs. In *Conference on Computer Vision and Pattern Recognition*, 2017.
- [35] M. Simonovsky and N. Komodakis. Graphvae: Towards generation of small graphs using variational autoencoders. *arXiv preprint arXiv:1802.03480*, 2018.
- [36] J. Straub, J. Chang, O. Freifeld, and J. Fisher III. A Dirichlet process mixture model for spherical data. In *Proceedings of the 18th International Conference on Artificial Intelligence and Statistics*, volume 38, pages 930–938, San Diego, CA, USA, 2015.
- [37] R. C. Wilson, E. R. Hancock, E. Pełkalska, and R. P. W. Duin. Spherical and hyperbolic Embeddings of data. *IEEE Transactions on Pattern Analysis and Machine Intelligence*, 36(11): 2255–2269, Nov. 2014. ISSN 0162-8828. doi: 10.1109/TPAMI.2014.2316836.
- [38] D. Zambon, L. Livi, and C. Alippi. Detecting changes in sequences of attributed graphs. In *IEEE Symposium Series on Computational Intelligence*, pages 1–7, Nov 2017. doi: 10.1109/SSCI.2017.8285273.

- [39] D. Zambon, C. Alippi, and L. Livi. Concept drift and anomaly detection in graph streams. *IEEE Transactions on Neural Networks and Learning Systems*, pages 1–14, Mar. 2018. doi: 10.1109/TNNLS.2018.2804443.
- [40] D. Zambon, L. Livi, and C. Alippi. Anomaly and change detection in graph streams through constant-curvature manifold embeddings. *arXiv preprint arXiv:1805.01360*, 2018.

Table 3: Summary of the iEEG datasets

Dataset	ID	Original ID	# graphs ( $Q_0$ )	# graphs ( $Q_1$ )	$N$
SDC	D1	Dog 2	1148	172	16
	D2	Dog 3	4760	480	16
	D3	Dog 4	2790	257	16
	D4	Patient 2	2990	151	16
	D5	Patient 5	2610	135	64
	D6	Patient 6	2772	225	30
	D7	Patient 7	3239	282	36
SPC	P1	Dog 2	500	42	16
	P2	Dog 3	1440	72	16
	P3	Dog 4	804	97	16

## Appendix A Datasets

**Delaunay triangulations** A graph is generated starting from its class support, by adding a Gaussian noise vector drawn from  $\mathcal{N}(0, 1)$ . The coordinates of the points are then used as node attributes ( $F = 2$ ), whereas the edge attributes are set to a constant value for each edge ( $S = 1$ ). For the nominal stream (class 0), we consider a support of seven points sampled from a uniform distribution in the  $[0, 10]$  interval on  $\mathbb{R}^2$ . Non-nominal classes are generated by perturbing each point of the support of class 0 with a noise vector sampled on the circumference of radius

$$\varrho = 10 \left( \frac{2}{3} \right)^{i-1}$$

where  $i$  is the index of the class. Class indices are proportional to the difficulty of detecting a change. We generate  $n = 5 \cdot 10^3$  graphs of class 0 for  $G_{train}$ , and consider 20 different operational streams, to evaluate the performance on increasingly difficult problems. Each operational stream consists of  $m = 2 \cdot 10^4$  graphs of classes 0 and  $i$ , with change point  $\tau = \frac{m}{2}$ .

**iEEG data** iEEG graphs are generated using the labeled training data available from Kaggle’s *UPenn and Mayo Clinic’s Seizure Detection Challenge* (SDC) and the *American Epilepsy Society Seizure Prediction Challenge* (SPC).<sup>3</sup> For the SDC datasets, we only consider subjects with more than 1000 labeled clips, while for SPC we consider those with more than 500 (due to the datasets of SPC being smaller overall, with some patients having as little as 42 labeled clips) Functional connectivity networks are generated for each one-second multivariate stream. The number of vertices corresponds to the number of variates in the stream. We initially filter the 60 Hz sub-band of the signals, and then adopt two measures of functional connectivity to generate edge attributes: 1) Pearson correlation and 2) the Directed Phase Lag Index (DPLI) [2]. In this paper, we only report the results obtained with Pearson correlation, as DPLI gave slightly worse results on average, but both could be used interchangeably (and, in principle, any other functional connectivity measure [2]). Functional connectivity is estimated in the high-theta band (70-100 Hz). As vertex attributes, we consider  $F = 4$  wavelet coefficients computed by means of discrete wavelet transform of the related signals. In order to sparsify the functional graphs, as a final preprocessing step we remove all edges with absolute value  $\leq 0.1$ . A summary of the SDC and SPC datasets is provided in Table 3. Like for the Delaunay triangulations, here we consider  $n = 5 \cdot 10^3$ ,  $m = 2 \cdot 10^4$ , and  $\tau = \frac{m}{2}$ . Since we have no way of synthesizing the graphs, we generate the training and operational streams via random bootstrapping.

## Appendix B Adversarial GAE

**GAE** For the encoder, we use two ECC layers of 32 and 64 channels respectively, with batch normalization, ReLU, and L2 regularization (with a factor of  $5 \cdot 10^{-4}$ ), followed by global attention pooling with 128 channels. The filter generating network for ECC layers consists of two fully connected ReLU layers of 128 units, with a linear output of  $F_l \cdot F_{l-1}$  neurons. The latent representation

<sup>3</sup>SDC: <https://www.kaggle.com/c/seizure-detection>; SPC: <https://www.kaggle.com/c/seizure-prediction>

is produced by a ReLU layer with 128 units followed by a linear layer with  $d + 1$  units (these last two layers are replicated in parallel in the case of the ensembled CCMs). The decoder is a fully connected three-layer network of 128, 256, and 512 neurons, with ReLU and batch normalization, followed by three parallel heads: a sigmoid layer for the adjacency matrix, and two linear layers for node and edge attributes. For subject P1 of the iEEG data, the configuration described above is prone to overfitting (probably due to the limited amount of samples available) and not able to reflect changes in the graph stream, so we add dropout between the ECC layers with probability 0.2 to mitigate the issue.

**Adversarial regularization** We consider a discriminator network with three ReLU layers of 128 units each, and a single-neuron sigmoidal output. For the prior, we use a manifold Gaussian  $\mathcal{N}_{\mathcal{M}_{\kappa_i}}(0, 1)$  (c.f. Section 2.2). When using the geometric critic we only need to choose the softness of the classification curve, set to  $\varsigma = 5$ .

**Training** We train all networks using Adam [15] with a learning rate of 0.001 and a batch size of 128. We normalize the node and edge attribute matrices of each graph node-wise, by removing the mean and scaling them to unit variance. For the GAE, we optimize (3), whereas in the regularization phase (when applicable) we train both  $D(\cdot)$  and  $D(\text{ENC}(\cdot))$  by minimizing the binary cross-entropy. We monitor the validation loss of the GAE for early stopping, using 10% of the training samples and a patience of 20 epochs.

## Appendix C Performance metric for CDTs

Accuracy is not a fair performance indicator for CDTs, as the temporal dynamics of a change may result in low true positive rates even if the change is consistently detected. To avoid this issue, we consider the *run lengths* (RLs) of the CDT, defined as the number of time-steps between two consecutive alarms. Given an operational stream where the change point is known, we consider the distributions of RLs in the nominal and non-nominal regimes and test whether nominal RLs are statistically larger than non-nominal ones according to the Mann-Whitney U test [24]. We then normalize the  $U$  statistic to obtain the Area Under the ROC (AUC) score, which in our case measures the separability of two RL distributions,

$$AUC_{RL} = \frac{U}{N_0 N_1}, \quad (7)$$

where  $N_0$  and  $N_1$  are the sample sizes of the measured RLs in the two regimes.

## Appendix D Full experimental results

We report in Tables 4 and 5 the results of all tested system configurations on the two application scenarios.

Table 4: AUC score on Delaunay triangulations for non-nominal classes 1-20 (results in bold are the best scores before rounding to two decimals).

CCM	CDT	Emb.	20	19	18	17	16	15	14	13	12	11
$\mathcal{M}_*$	D-CDT	Geom.	0.49	0.51	0.50	0.58	0.51	0.58	0.64	0.61	0.56	0.59
		Prior	0.52	0.49	0.52	0.57	0.52	0.55	0.58	0.58	0.53	0.61
	R-CDT	Geom.	<b>0.70</b>	<b>0.74</b>	<b>0.71</b>	<b>0.75</b>	<b>0.74</b>	<b>0.77</b>	<b>0.76</b>	<b>0.75</b>	<b>0.78</b>	<b>0.77</b>
		Prior	0.42	0.05	0.24	0.30	0.32	0.39	0.21	0.33	0.28	0.39
$\mathcal{M}_{-1}$	D-CDT	Geom.	0.49	0.52	0.55	0.53	0.54	0.54	0.61	0.55	0.59	0.57
		Prior	0.52	0.46	0.55	0.55	0.49	0.56	0.63	0.51	0.55	0.58
	R-CDT	Geom.	0.47	0.51	0.52	0.55	0.55	0.61	0.64	0.59	0.59	0.67
		Prior	0.48	0.46	0.53	0.55	0.54	0.65	0.63	0.53	0.58	0.62
$\mathcal{M}_0$	D-CDT	Geom.	0.55	0.43	0.45	0.50	0.50	0.65	0.73	0.60	0.60	0.64
		Prior	0.54	0.63	0.61	0.61	0.51	0.61	0.66	0.59	0.57	0.65
	R-CDT	Geom.	0.53	0.55	0.54	0.57	0.54	0.60	0.56	0.59	0.60	0.63
		Prior	0.49	0.51	0.51	0.53	0.49	0.54	0.52	0.50	0.50	0.55
$\mathcal{M}_1$	D-CDT	Geom.	0.37	0.47	0.53	0.47	0.45	0.43	0.48	0.49	0.48	0.50
		Prior	0.47	0.52	0.55	0.54	0.49	0.57	0.61	0.56	0.53	0.57
	R-CDT	Geom.	0.42	0.51	0.53	0.53	0.49	0.51	0.53	0.54	0.55	0.61
		Prior	0.45	0.51	0.50	0.53	0.53	0.62	0.59	0.62	0.55	0.59
-	D-CDT	[39]	0.49	0.49	0.50	0.49	0.50	0.50	0.50	0.49	0.50	0.50

CCM	CDT	Emb.	10	9	8	7	6	5	4	3	2	1
$\mathcal{M}_*$	D-CDT	Geom.	0.51	0.70	0.91	0.93	0.79	0.98	1.00	1.00	1.00	1.00
		Prior	0.50	0.63	0.94	0.97	0.95	0.99	1.00	1.00	1.00	1.00
	R-CDT	Geom.	<b>0.73</b>	0.82	<b>0.98</b>	<b>0.99</b>	<b>0.96</b>	<b>1.00</b>	<b>1.00</b>	<b>1.00</b>	1.00	<b>1.00</b>
		Prior	0.20	0.43	0.55	0.73	0.72	0.73	<b>1.00</b>	<b>1.00</b>	<b>1.00</b>	<b>1.00</b>
$\mathcal{M}_{-1}$	D-CDT	Geom.	0.48	0.68	0.71	0.92	0.53	0.75	0.96	0.93	0.90	1.00
		Prior	0.43	0.58	0.61	0.67	0.75	0.86	1.00	0.89	0.96	1.00
	R-CDT	Geom.	0.60	0.85	0.91	0.99	0.95	0.98	0.99	1.00	1.00	1.00
		Prior	0.39	0.87	0.96	0.98	0.55	<b>1.00</b>	1.00	1.00	0.93	0.98
$\mathcal{M}_0$	D-CDT	Geom.	0.47	0.59	0.31	0.88	0.40	0.46	0.99	0.99	0.99	0.99
		Prior	0.58	0.59	0.63	0.88	0.67	0.76	1.00	1.00	0.93	1.00
	R-CDT	Geom.	0.58	0.69	0.65	0.86	0.62	0.77	0.94	0.94	0.94	0.94
		Prior	0.43	0.60	0.71	0.74	0.66	0.84	0.96	0.96	0.96	0.96
$\mathcal{M}_1$	D-CDT	Geom.	0.53	0.54	0.68	0.79	0.83	0.79	0.76	0.97	0.90	0.86
		Prior	0.51	0.59	0.59	0.75	0.72	0.70	0.90	0.90	0.89	0.90
	R-CDT	Geom.	0.56	0.76	0.85	0.92	0.80	0.91	0.92	1.00	1.00	1.00
		Prior	0.50	<b>0.91</b>	0.79	0.98	0.77	0.98	1.00	1.00	0.99	1.00
-	R-CDT	[39]	0.52	0.62	0.56	0.57	0.88	0.91	0.93	0.93	0.93	0.93

Table 5: AUC score on iEEG data (results in bold are the best scores before rounding to two decimals).

CCM	CDT	Emb.	D1	D2	D3	D4	D5	D6	D7	P1	P2	P3
$\mathcal{M}_*$	D-CDT	Geom.	0.99	0.99	0.99	0.93	0.99	0.66	0.99	0.22	0.19	0.87
		Prior	0.98	0.99	0.99	0.92	0.99	0.43	0.98	0.10	0.15	0.83
	R-CDT	Geom.	<b>1.00</b>	<b>1.00</b>	<b>1.00</b>	0.94	<b>1.00</b>	0.74	<b>1.00</b>	0.54	0.51	0.97
		Prior	1.00	1.00	1.00	<b>0.96</b>	1.00	0.79	0.98	0.40	0.45	<b>0.98</b>
$\mathcal{M}_{-1}$	D-CDT	Geom.	<b>1.00</b>	0.99	0.99	0.94	0.99	0.62	<b>1.00</b>	0.64	0.25	0.90
		Prior	0.99	0.99	0.99	0.90	0.99	0.34	0.95	0.78	0.16	0.92
	R-CDT	Geom.	0.99	0.99	0.99	0.93	0.98	0.85	0.99	0.25	0.28	0.90
		Prior	0.97	0.99	0.97	0.83	0.98	0.82	0.96	0.58	0.28	0.95
$\mathcal{M}_0$	D-CDT	Geom.	0.99	0.99	0.99	0.81	0.99	0.00	0.99	0.44	0.09	0.78
		Prior	0.99	0.99	0.99	0.74	0.97	0.59	0.99	0.76	0.10	0.85
	R-CDT	Geom.	0.92	0.96	0.93	0.83	0.97	0.61	0.93	0.17	0.17	0.74
		Prior	0.91	0.93	0.88	0.62	0.97	0.71	0.96	0.15	0.53	0.65
$\mathcal{M}_1$	D-CDT	Geom.	0.99	0.99	0.99	0.94	0.88	0.65	0.89	0.67	0.15	0.91
		Prior	0.99	0.99	0.99	0.90	0.99	0.33	0.98	<b>0.87</b>	0.48	0.82
	R-CDT	Geom.	0.99	0.99	0.99	<b>0.96</b>	0.99	0.85	0.97	0.57	0.20	0.95
		Prior	0.99	0.99	0.99	0.95	0.99	0.53	0.99	0.64	0.73	0.91
$\mathcal{M}_0$	R-CDT	[39]	0.92	0.74	0.84	0.90	0.90	<b>0.88</b>	0.79	0.73	<b>0.84</b>	0.90